RSC Advances

PAPER

View Article Online
View Journal | View Issue

Cite this: *RSC Adv.*, 2022, **12**, 27154

AC conductivity and phase transition of the BST–BFO ceramic doped with Yb

M. Ben Abdessalem, *[a] S. Chkoundali,[a] A. Oueslati [b] and A. Aydi[a]

The homogeneity of the $0.8(Ba_{0.8}Sr_{0.2})TiO_3$–$0.2(Bi_{0.85}Yb_{0.15})FeO_3$ ceramic, prepared by a solid-state process, was studied and quantitatively analyzed by scanning electron microscopy (SEM) and energy dispersive X-ray spectroscopy (EDX). At ambient temperature, X-ray diffraction shows the existence of only one perovskite phase in the tetragonal structure with the space group *P4mm*. The thermal variations of ε'_r (real part of the dielectric permittivity) for this composition show extended peaks with temperature; this broadening of the peaks can be attributed to the diffuse character of the transition. As the frequency increases, T_m (temperature of maximum permittivity) moves at higher temperatures, and the maximum values of ε'_r decrease. Moreover, the impedance spectra ($-Z''$ *vs.* Z') show the presence of two arcs of circles that have been modeled with an equivalent electrical circuit. The arcs of the circles centered under the real axis (Z) prove the Cole–Cole-type behavior. Each circle is associated with either the grain effect or grain boundaries. Electrical modulus analysis shows that the capacitance of the ceramic is enhanced, which is in good agreement with the results of complex impedance analysis. The AC conductivity complies with the universal power law. It disputes the modification of AC conductivity by adopting the Arrhenius-type of electrical conductivity. The temperature dependence of alternating current conductivity (σ_g) and direct current conductivity (σ_{DC}) confirms the existence of the ferroelectric–paraelectric phase transition.

Received 30th May 2022
Accepted 8th September 2022

DOI: 10.1039/d2ra03371b

rsc.li/rsc-advances

1. Introduction

Ferroelectric materials are very interesting due to their simple crystalline structure. They are widely used in electronics, microelectronics and electromechanical transducers[1,2] due to their piezoelectric, dielectric and thermoelectric properties.[3,4]

The physical properties of the ferroelectric material $Ba_{0.8}Sr_{0.2}TiO_3$ (BST) confer an increase in its dielectric constant of about 12 000 and a transition temperature T_C of 340 K.[5,6] $BiFeO_3$ (BFO) is a multiferroic material that exhibits both ferroelectric and antiferromagnetic orders. Its structure is a rhombohedral distorted perovskite (space group *R3c*)[7] described by a rising Curie temperature ($T_C = 1103$ K) and an antiferromagnetic Neel temperature ($T_N = 643$ K (ref. 8)) and a spin that has been spiral modulated.[9,10] In order to promote the properties of the BFO compound and reduce its defects, *i.e.* extreme current losses and high coercive fields,[10] various tests have been effective, including the ion substitution test.

It has been observed in the literature that partial substitution in BFO-based ceramics by rare earths such as La,[11] Pr,[12] Nd,[13,14] Gd,[15] Dy[16] and Ho[17] at the Bi site cause a structural modification and improve the ferroelectric and ferromagnetic properties of the substituted materials. Indeed, the conductivity, ferroelectricity and magnetization are well improved, which makes the obtained compounds more useful in storage applications. In addition, Ilic *et al.*[18] proved that yttrium upgrades the electric and magnetic properties.

In this paper, the main objective of our research work is to study the preliminary structural and electrical properties of BFO by ytterbium (Yb) doping in order to obtain information on the selection of materials for certain significant applications. Similarly, for this reason, we synthesized the compound $0.8(Ba_{0.8}Sr_{0.2})TiO_3$–$0.2(Bi_{0.85}Yb_{0.15})FeO_3$ (BST–BiYbFO) by the solid-state method. This compound was characterized by scanning electron microscopy (SEM), energy dispersive X-ray spectroscopy (EDX) and complex impedance spectroscopy.

2. Experimental

Polycrystalline samples of (BST–BiYbFO) were prepared by adopting the classic solid-state reaction. The starting reagents $BaCO_3$, $SrCO_3$, Bi_2O_3, TiO_2, Fe_2O_3 and Yb_2O_3 were of high purity (up to 99.9% purity, Aldrich).

These precursors were ground in a planetary mill for 2 hours (h) in ethanol to homogenize the solution and reduce the particle size; the powders obtained were calcined at 770 °C for

[a]*Laboratory of Multifunctional Materials and Applications (LaMMA), LR16ES18, Faculty of Sciences, University of Sfax, B. P. 1171, 3000 Sfax, Tunisia. E-mail: ben.abdessalem.manel@gmail.com*

[b]*Condensed Matter Laboratory, Faculty of Sciences, University of Sfax, B. P. 1171, 3000 Sfax, Tunisia*

3 h. The resulting solution was ground again and pelleted under 3 ton per cm^2 and finally sintered at 970 °C for 3 h.

At room temperature (RT), X-ray diffraction (XRD) patterns were obtained on a Siemens D5000 diffractometer using Cu K emission = 1.5460 Å in the angular range of $10° < 2\theta < 80°$ with 10 s for each step of 0.02° around the structure to determine the composition. The FullProf[19–21] software was used to analyze the XRD profiles. The morphologies and sizes of the samples were studied directly with a Hitachi SU70 Merlin SEM at an acceleration voltage of 3 kV, equipped with an EDXS energy-dispersive X-ray spectrometer, which was used for the elemental analysis of the different phases. For electrical measurements, the BST–BiYbFO powder was pressed into disks about 8 mm in diameter and 1 mm thick. The electrical properties were measured by an impedance analyzer (TEGAM 3550) in the temperature and frequency ranges of 473–753 K and 100 Hz–2 MHz, respectively.

3. Results and discussion

3.1. X-ray, SEM and EDX characterization

Fig. 1 shows the XRD pattern of the compound BST–BiYbFO recorded at RT. The peaks were successfully indexed using the FullProf program in the tetragonal system with the space group *P4mm*. The parameters were $a = b = 3.9737$ Å, $c = 3.9840$ Å, $\alpha = \beta = \gamma = 90°$ and $V = 62.9085$ $Å^3$, with a reliability factor of $\chi_i^2 = 2.91$, which is consistent with the literature.[22]

Analysis of the synthesized powders by XRD and SEM allows us to control the formation of the desired phase and the solid solution boundaries.[23] These additional studies can distinguish the elements or phases present in our compound through the detection of backscattered electrons. From the SEM micrographs in Fig. 1 (with a resolution of 2 μm (top) and 5 μm (bottom)), it can be seen that the sample consists of uniform grains with a dimension of about 3.5 μm. It is also observed that the grains are compactly distributed over the surface with some porosity present.

Table 1 : Quantitative analysis of the $0.8(Ba_{0.8}Sr_{0.2})TiO_3$–$0.2(Bi_{0.85}Yb_{0.15})FeO_3$ ceramic

Elements	Weight %	Atomic %
O	19.79	54.99
Ti	26.17	24.3
Fe	5.03	4
Sr	7.57	3.84
Ba	35.56	11.51
Yb	4.54	1.17
Bi	0.9	0.19
Total	99.56	100

The corresponding EDX[24] analysis confirms that all elements are present in the material (Table 1), as indicated in Fig. 2. In addition to the presence of Ba, Sr, Bi, Fe and O, the spectra clearly show the successful Yb doping in BST–BFO. No other impurities were found in the EDX analysis, confirming the clarity of the sample.

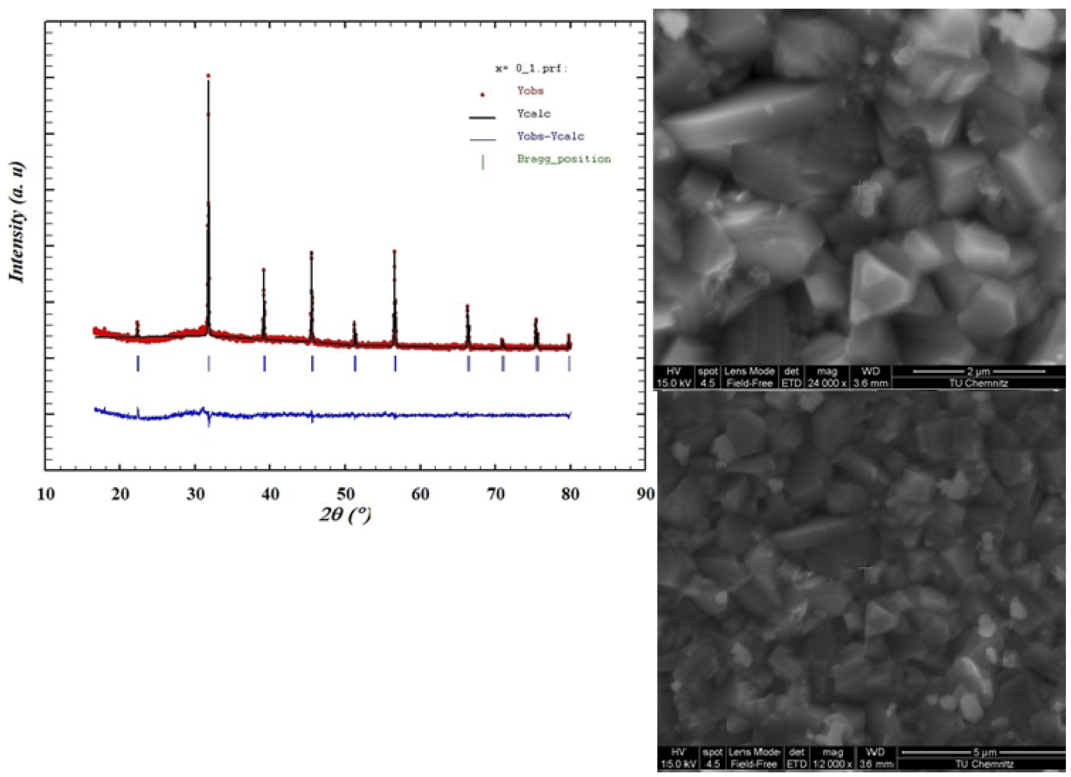

Fig. 1 XRD pattern for the tetragonal ceramic $0.8(Ba_{0.8}Sr_{0.2})TiO_3$–$0.2(Bi_{0.85}Yb_{0.15})FeO_3$ at room temperature and SEM micrographs of the ceramic surface.

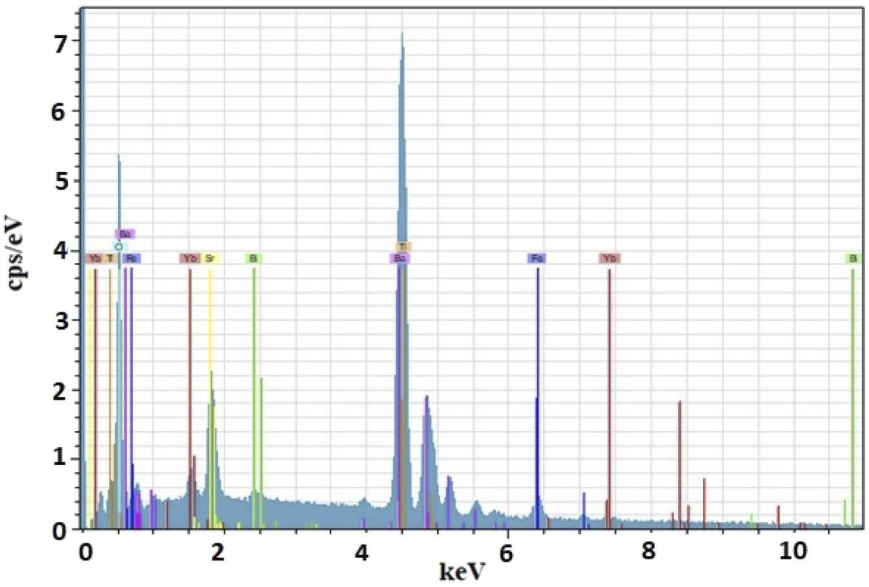

Fig. 2 The EDAX spectrum of the $0.8(Ba_{0.8}Sr_{0.2})TiO_3$–$0.2(Bi_{0.85}Yb_{0.15})FeO_3$ ceramic.

3.2. Dielectric study

Investigation of the dielectric allows for the determination of the ferroelectric phase transition temperature and the nature of the relaxing ferroelectric behavior of BST–BiYbFO.

Fig. 3(a) shows the variation of the real component of the dielectric permittivity (ε'_r) with frequency. As the frequency increases, ε'_r continues to decrease. For high temperatures, *i.e.* at 693 K, ε'_r is about 6200 at 125 Hz and then becomes more or less stabilized down to above 10 MHz. The maximum value of ε'_r changes with frequency, leading to a dispersion effect. Two plateaus are observed, with one occurring in the lower-frequency region (10^2–10^4 Hz) and another in the higher-

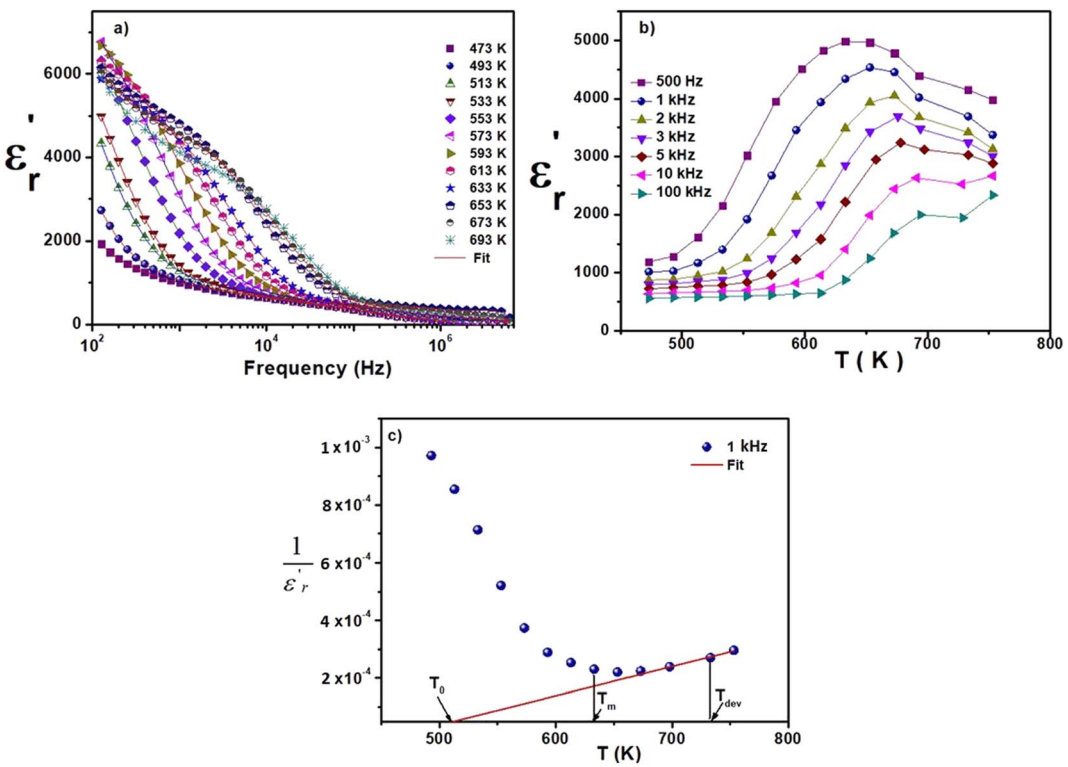

Fig. 3 (a) Frequency variation of the dielectric constant (ε'_r) at different temperatures. (b) Temperature dependence of the permittivity ε'_r for BST–BFO. (c) The variation of $\frac{1}{\varepsilon'_r}$ *versus* temperature for the $0.8(Ba_{0.8}Sr_{0.2})TiO_3$–$0.2(Bi_{0.85}Yb_{0.15})FeO_3$ ceramic.

frequency region (10^4–10^6 Hz) for all the measured temperatures. For electronic ceramics, both grains and grain boundaries provide non-ignorable effects on the electrical properties.

In fact, at lower frequencies, the pattern can be attributed to various types of polarizations in which the space charges are able to follow the frequency of the applied field given that they have enough time. These space charges are generally concentrated in the grain boundaries. On the contrary, at higher frequencies, these space charges do not have sufficient time to undergo relaxation;[25,26] it is the effect of the grains that intervenes in this case. High values of dielectric permittivity are observed only at high temperatures and very low frequencies, which may be due to the free charge build-up at interfaces within the bulk of the sample (interfacial Maxwell–Wagner polarization)[27] and the interface between the sample and the electrodes (space charge polarization). These results are similar to those found by Patil *et al.*[28]

Fig. 3(b), showing the temperature (T) dependence of the real part of the dielectric constant (ε'_r) at different frequencies, proves the existence of a plateau at low temperatures, which can be described as a grain or bulk response of the LBFO compound. As the frequency increases, T_m (the temperature of the maximum value of permittivity) moves toward high temperatures and the maximum values of ε'_r decrease. In addition, a large scatter in the evolution of ε'_r under T_m was observed. This behavior shows the relaxing character of this material. The value of ε'_r increases with temperature to a certain degree and shows a broad dielectric extreme at a certain temperature, $T_m = 633$ K, which is attributed to the phase transition from an antiferroelectric to a paraelectric state.[29–34]

The thermal variation of $1/(\varepsilon'_r)$ for this compound, presented in Fig. 3(c), shows a deviation from the Curie–Weiss law given by the equation:[35]

$$\varepsilon'_r = \frac{C}{T - T_0} \quad T > T_C$$

Further theoretical fitting shows that in this case, the transition is diffuse and that the behavior is of the relaxor type. This is a second-order transition, where C is the Curie–Weiss constant and T_0 is the Curie–Weiss temperature. Since ion diffusion occurs with increasing temperature, the movement of T_C (*i.e.* the transition from the antiferroelectric to the paraelectric state) at high temperatures is most likely due to space charge polarization.[36–39]

3.3. Impedance analysis

The behavior of the impedance spectra for different materials is often explained using Argand diagrams (Cole–Cole or Nyquist). In fact, these diagrams are particularly useful for materials that represent one or more relaxation processes, are better separated, and are comparable considering the functional forms of Debye or Cole–Cole.[40–45]

Fig. 4(a) presents the Nyquist diagrams ($-Z'' = f(Z')$) for BST–BiYbFO for different temperatures (473–753 K). The experimental points of these curves are based on circular arcs that

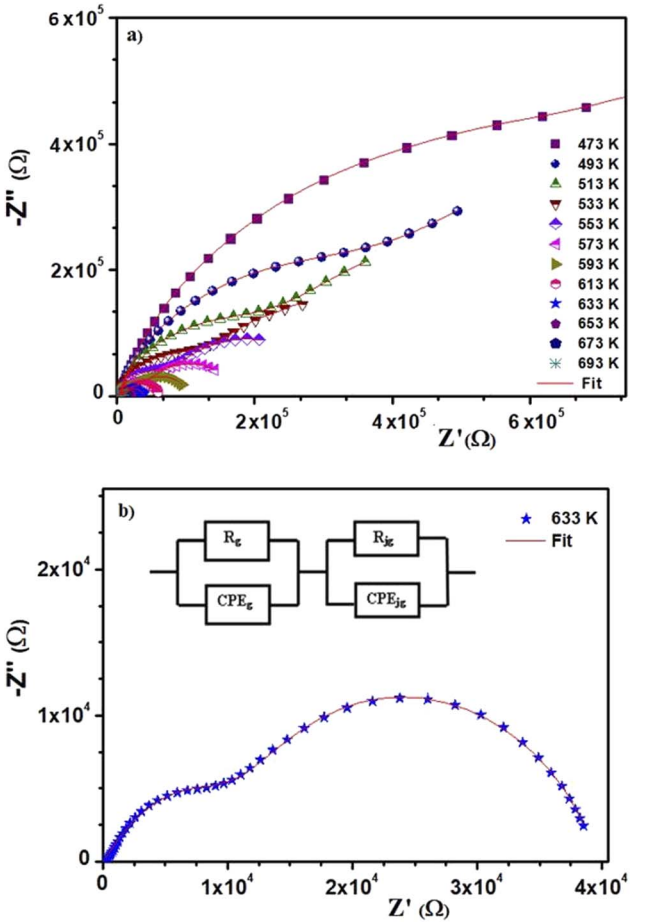

Fig. 4 (a) Complex impedance plot at different temperatures of $0.8(Ba_{0.8}Sr_{0.2})TiO_3$–$0.2(Bi_{0.85}Yb_{0.15})FeO_3$. (b) Impedance diagrams at 633 K.

pass near the origin and have their centers below the real axis. Since the Debye plots produce semicircles centered on the real axis, this shows that the behavior of this material follows the Cole–Cole model. Any increase in temperature is accompanied by a decrease in resistance, which shows the thermal activation of the conductivity of the material. We examined the thermal evolution of the impedance plots of the BST–BiYbFO compound to verify the assignment of the grain boundaries to the high-temperature dielectric anomaly. With increasing temperature (Fig. 4(b)), the positions of the different frequencies shift from the grain semicircle (higher frequencies) to the grain boundary semicircle (lower frequencies). The anomaly observed at high temperatures could therefore be related to the oxygen vacancies present at the grain boundaries.[46–49] By modeling the impedance spectra, a resistive effect of the grain boundaries greater than that of the reinforcements could be demonstrated. This confirms that this dielectric anomaly is mainly due to the oxygen vacancies associated with the grain boundaries. In order to explain the electrical behavior of the material, we prepared an equivalent circuit (inset in Fig. 4(b)) formed from a series of combinations of grains (g) and grain boundaries (gb).

The first consists of a parallel combination of resistance (R_g) and fractal capacitance (CPE_g) with the impedance $Z_{CPE} =$

Table 2 Extracted parameters for the circuit elements of the BST–BFO compound

T (K)	R_g (Ω)	CPE$_g$ (10^{-8} F)	α_g	R_{gb} (Ω)	CPE$_{gb}$ (10^{-9} F)	α_{gb}
473	1 726 700	1.672	0.684	202 770	1.67	0.9245
493	1 343 100	3.553	0.644	247 100	1.807	0.904
513	1 051 200	5.193	0.6188	145 570	1.719	0.897
533	685 380	7.484	0.5762	64 444	0.981	0.86
553	407 060	8.982	0.5675	35 420	0.8791	0.872
573	52 061	0.550	0.756	111 340	12.038	0.901
593	30 439	0.563	0.755	70 369	13.228	0.883
613	18 796	0.726	0.732	42 344	1.333	0.879
633	16 098	0.236	0.652	21 802	87.510	0.869
653	5670	0.356	0.807	15 401	1.353	0.868
673	5125	1.810	0.716	8935	11.790	0.853
693	3395	1.967	0.675	6254	13.146	0.843

$Q(i\omega)^{-\alpha}$ (ref. 41) (where Q is a positive constant and a positive number less than or equal to 1), while the second consists of a parallel combination of resistance (R_{gb}) and a constant phase element (CPE$_{gb}$). The values of the fitted parameters extracted from the equivalent circuit model are summarized in Table 2.

The real and imaginary parts of the complex impedance are expressed by:

$$Z' = ([R_g + R_g^2 Q_g \omega^{\alpha_g} \cos(\alpha_g \pi/2)]/([1 + R_g Q_g \omega^{\alpha_g} \cos(\alpha_g \pi/2)]^2 + [R_g Q_g \omega^{\alpha_g} \sin(\alpha_g \pi/2)]^2)) + ([R_{gb} + R_{gb}^2 Q_{gb} \omega^{\alpha_{gb}} \cos(\alpha_{gb} \pi/2)]/([1 + R_{gb} Q_{gb} \omega^{\alpha_{gb}} \cos(\alpha_{gb} \pi/2)]^2 + [R_{gb} Q_{gb} \omega^{\alpha_{gb}} \sin(\alpha_{gb} \pi/2)]^2)) \quad (1)$$

$$Z'' = ([R_g^2 Q_g \omega^{\alpha_g} \sin(\alpha_g \pi/2)]/([1 + R_g Q_g \omega^{\alpha_g} \cos(\alpha_g \pi/2)]^2 + [R_g Q_g \omega^{\alpha_g} \sin(\alpha_g \pi/2)]^2)) + ([R_{gb}^2 Q_{gb} \omega^{\alpha_{gb}} \sin(\alpha_{gb} \pi/2)]/([1 + R_{gb} Q_{gb} \omega^{\alpha_{gb}} \cos(\alpha_{gb} \pi/2)]^2 + [R_{gb} Q_{gb} \omega^{\alpha_{gb}} \sin(\alpha_{gb} \pi/2)]^2)) \quad (2)$$

The variation of the real part of the impedance (Z') as a function of frequency for the BST–BiYbFO composition is plotted in Fig. 5(a) for different temperatures. It can be seen that Z' decreases with increasing temperature and frequency, leading to an increase in electrical conduction in the sample depending on these parameters. High values of Z' are obtained at low frequencies and low ones correspond to high frequencies (>10^6 Hz). This behavior could be explained by the presence of space charges and/or ionic conduction.[50–53] At high and medium frequencies, Z' is independent of temperature, which reduces the influence of space charges.[54] In fact, in the highest frequency range, all the curves merge and become independent of frequency, suggesting a possibility of space charge release.[53]

Fig. 5(b) shows the change in the imaginary part of the impedance (Z'') with frequency for the BST–BiYbFO composition at different temperatures. At higher frequencies and higher temperatures, the Z''_{max} peaks change and broaden, indicating relaxation in the studied composition. This curve is useful to evaluate the relaxation frequency in materials with resistive character.[55] The asymmetrical broadening of the peak under the influence of temperature suggests a temperature-dependent distribution of relaxation times.[56]

3.4. AC conductivity studies

Fig. 6 shows the frequency dependence of electrical conductivity (AC) at different temperatures. The conductivity model is represented by two distinct regions. First, the conductivity in the low-frequency range is frequency independent, which characterizes the direct conductivity due to the displacement of the

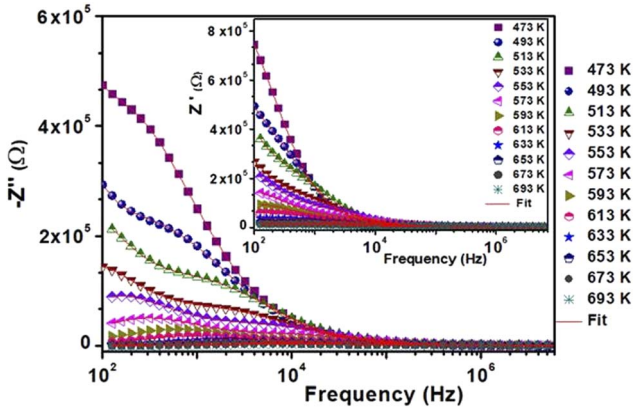

Fig. 5 Variation of the real part Z' and the imaginary part $-Z''$ of the impedance as a function of frequency at various temperatures.

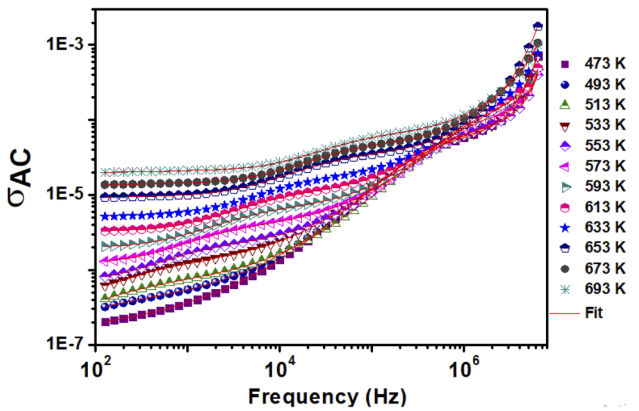

Fig. 6 Variation of the AC conductivity (σ_{AC}) with frequency at selected temperatures of 0.8($Ba_{0.8}Sr_{0.2}$)TiO_3–0.2($Bi_{0.85}Yb_{0.15}$)FeO_3.

charge carriers.[57] Second, the AC conductivity–compatible dispersion regime occurs at a higher frequency.[58]

Jonscher's law is commonly used to explain the phenomenon of conductivity dispersion:[42,59,60]

$$\sigma_{AC}(\omega) = \sigma_{DC} + A\omega^{S} \quad (3)$$

where DC denotes DC conductivity, A is a temperature-dependent constant, and S denotes the degree of mobile ion interaction.[61]

From these curves, we can see that Jonscher's classical equation (eqn (3)) does not explain the behavior of our experimental data. Using eqn (4) agrees better with the experimental values and the developed equation is called the Jonscher equation.[62]

$$\sigma_{AC}(\omega) = \frac{\sigma_S}{1+(\tau\omega)^2} + \frac{\sigma_\infty(\tau\omega)^2}{1+(\tau\omega)^2} + A\omega^{S} \quad (4)$$

where S is the conductivity at low frequencies, σ_∞ is a high-frequency estimate, and τ denotes the characteristic relaxation time.

3.5. DC electrical conductivity

Electrical conductivity depends on the slightly bound charged particles that move through a material under the effect of a continuous electric field. The following relationship can be used to calculate electrical conductivity (DC) from resistance (R):

$$\sigma_{DC} = \frac{e}{S \times R} \quad (5)$$

where e and S respectively are the thickness and the surface of the pellet and R is the resistance determined by the fit of the curve $-Z'' = f(Z')$. The variation of $\ln(\sigma_{DC} \times T)$ *versus* $1000/T$ is plotted in Fig. 7. The Arrhenius law[63] describes the study of DC conductivity as follows:

$$\sigma_{DC} \times T = A \exp\left(\frac{-E_a}{K_B T}\right) \quad (6)$$

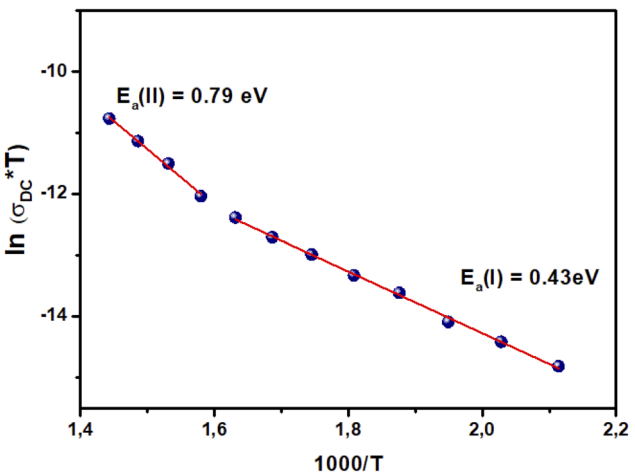

Fig. 7 Temperature dependence of $\ln(\sigma_{DC} \times T)$.

where A is the pre-exponential factor, K_B is the Boltzmann constant and E_a is the activation energy. The activation energy has been deduced from a linear adjustment at the data points. The phase transition is determined by the change of the curve's slope at 633 K. In the ferroelectric zone, the activation energy is $E_I = 0.44$ eV, while in the paraelectric region, it is $E_{II} = 0.68$ eV. This behavior is also common to semiconductor oxides and perovskites,[64,65] where there is usually a change in the low-temperature conduction mechanism.

3.6. Modulus

Macedo *et al.* first developed the modulus formalism in 1972.[66] This formalism has been applied to the study of material electrical characteristics. It is used to determine the relaxation times of the conductivity. The complex modulus is expressed as:

$$M^* = j\omega C_0 Z = M' + jM'' \quad (7)$$

Fig. 8 shows the variation of the imaginary part M'' of the complex modulus as a function of the real part M' at different temperatures. The influence of grains and grain boundaries is related to the two observed semicircles, consistent with previous findings.

Fig. 8(a) shows the change in the real part M' of the electrical modulus as a function of frequency at different temperatures. It is observed that, at low frequencies, the values of M' are very low

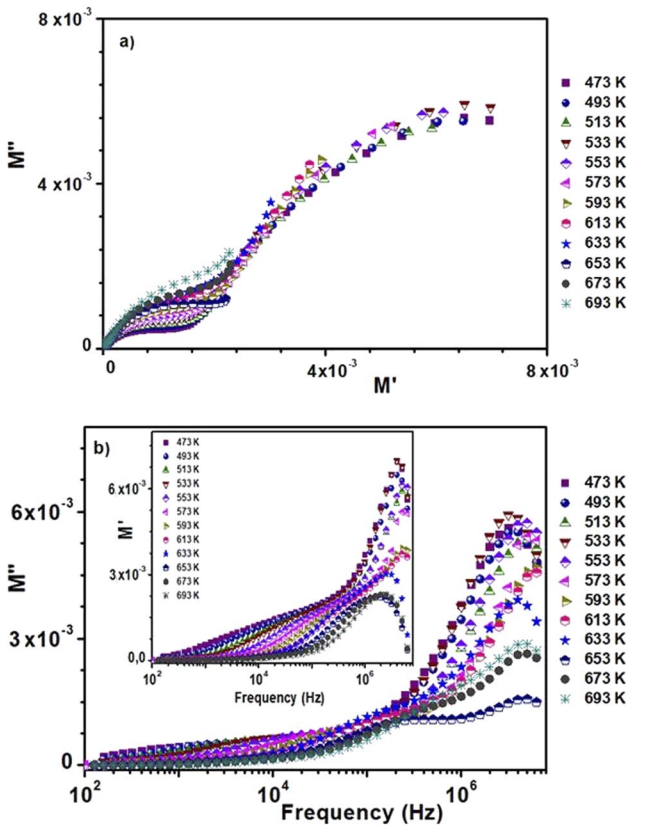

Fig. 8 (a) Argand plot of $0.8(Ba_{0.8}Sr_{0.2})TiO_3$–$0.2(Bi_{0.85}Yb_{0.15})FeO_3$. (b) Spectroscopy plots of the M' and M'' curves.

(from 10^6 Hz). The spectra of M' present rapid decreases according to the equation: $M' = \varepsilon'/(\varepsilon'^2 + \varepsilon''^2)$. Moreover, the increase in M' is due to the accumulation of charges at the electrode–electrolyte interface, *i.e.* it is space charge polarization.[67,68]

The fluctuation of the imaginary part M'' of the electrical modulus as a function of frequency at various temperatures is shown in Fig. 8(b). These fluctuations are found in two temperature ranges: $T < 633$ K and $T > 633$ K. This confirms the existence of the two conduction domains. In the first domain, the maxima of the curves are not of the same levels, and in the second domain, the maxima of the curves decrease when the temperature increases. Moreover, these spectra present asymmetrical relaxation peaks whose maxima shift towards high frequencies when the temperature increases.[69,70]

4. Conclusion

In this study, the interaction of the structure and electrical properties of the BST–BiYbFO ceramic prepared by solid-state technology has been studied.

According to X-ray diffraction, the sample shows a tetragonal structure with a space group of *P*4*mm*. Dielectric measurement showed a relaxing ferroelectric behavior at the phase transition temperature of 633 K. The analysis of the impedance Z' as a function of Z'' shows two semicircles that were modeled by a simple equivalent circuit.

The two relaxation peaks in the modulus spectra represent the input of grains and grain boundaries to the electrical response. With increasing temperature, electrical modulus and impedance measurements showed a relaxing effect shifting to higher frequencies.

For AC conductivity, the law of universal power states that $\sigma_{AC}(\omega) = \sigma_{DC} + A\omega^S$. Activated Arrhenius-type electrical transport mechanisms are responsible for the linear variation in DC conductivity. The frequency-dependent conductivities of the title compound show two distinct linear zones: $E_I = 0.44$ eV in region I ($T < T_C$) and $E_{II} = 0.68$ eV in region II ($T > T_C$). This shows that the presence of oxygen is the main cause of electrical conduction in BST–BiYbFO.

Conflicts of interest

Authors declare that they have no conflict of interest or personal relationships that could have appeared to influence the work reported in this paper.

References

1 G. F. Teixeira, T. R. Wright, D. C. Manfroi, E. Longo, J. A. Varela and M. A. Zaghete, *Mater. Lett.*, 2015, **139**, 443.
2 M. Ben Abdessalem, S. Aydi, A. Aydi, N. Abdelmoula, Z. Sassi and H. Khemakhem, *J.Applied Physics A.*, 2017, **123**, 583.
3 A. S. Bhalla, R. Guo and R. Roy, *Mater. Res. Innovations*, 2000, **4**, 3.
4 C. D. Chandler, C. Roger and M. J. H Smith, *Chem. Rev.*, 1993, **93**, 1205.
5 L. BenAbdessalem, M. BenAbdessalem, A. Aydi and Z. Sassi, *J. Mater. Sci.: Mater. Electron.*, 2017, **28**, 14264–14270.
6 H. Abdelkefi, H. Khemakhem, G. Velu, J. C. Carru and R. V. Muhll, *J. Alloys Compd.*, 2005, **399**, 1.
7 S. Kongtaweelert, D. C. Sinclair and S. PanichphantCurr, *Appl. Phys.*, 2006, **6**, 474.
8 P. Fischer, M. Polomska, I. Sosnowska and M. Szymanshi, *J. Phys. C*, 1980, **13**, 1931–1940.
9 B. Wodecka-Dus and D. Czekaj, *Arch. Metall. Mater.*, 2011, **56**, 1127.
10 G. Catalan and J. F. Scott, *Adv. Mater.*, 2009, **21**, 2463.
11 S.-T. Zhang, Y. Zhang, M.-H. Lu, *et al.*, *Appl. Phys. Lett.*, 2006, **88**, 3.
12 D. Varshney, P. Sharma, S. Satapathy and P. K. Gupta, *J. Alloys Compd.*, 2014, **584**, 232–239.
13 G. L. Yuan, S. W. Or, J. M. Liu and Z. G. Liu, *Appl. Phys. Lett.*, 2006, **89**, 052905.
14 G. L. Yuan and S. W. Or, *Appl. Phys. Lett.*, 2006, **88**, 062905.
15 V. A. Khomchenko, D. A. Kiselev, I. K. Bdikin, *et al.*, *Appl. Phys. Lett.*, 2008, **93**, 262905.
16 V. A. Khomchenko, D. V. Karpinsky, A. L. Kholkin, *et al.*, *J. Appl. Phys.*, 2010, **108**, 074109.
17 N. Jeon, D. Rout, W. Kim and S. L. Kang, *Appl. Phys. Lett.*, 2011, **98**, 072901.
18 N. I. Ilic, J. D. Bobic, B. S. Stojadinovic, A. S. Dzunuzovic, M. M. Vijatovic Petrovic, Z. D. Dohcevic-Mitrovic and B. D. Stojanovic, *J. Mater. Res. Bullet.*, 2016, **77**, 60–69.
19 T. Roismel and J. Rodriguez-Carvajal, *CNRS-Université de rennes. Laboratoire Brillouin (CEA-CNRS), version 3.70, May 2004*, LLB-LCSIM, 2005.
20 M. ben Abdessalem, A. Aydi, Z. Sassi, L. Seveyrat, V. Perrin, N. Abdelmoula, H. Khemakhem and L. Lebrun, *J. Appl. Phys.*, 2021, **127**, 80.
21 H. M. Rietfeld, *J. Appl. Crystallogr.*, 1969, **2**, 65–71.
22 H. Ghoudi, S. Chkoundali, A. Aydi and K. Khirouni, *Appl. Phys. A*, 2017, **123**, 703.
23 D. A. Samuelson, Energy dispersive X-ray microanalysis, *Methods Mol. Biol.*, 1998, **108**, 413–424.
24 Z. Mohamed, E. Tka, J. Dhahri, *et al.*, *J. Alloys Compd.*, 2014, **615**, 290–297.
25 J. Liu, X. Q. Liu and X. M. Chen, *J. Appl. Phys.*, 2016, **119**, 204102.
26 H. O. Rodrigues, G. F. M. Pires Junior, J. S. Almeida, E. O. Sancho, A. C. Ferreira, M. A. S. Silva and A. S. B. Sombra, *J. Phys. Chem. Solids*, 2010, **71**, 1329.
27 X. J. Xi, S. Y. Wang, W. F. Liu, H. J. Wang, F. Guo, X. Wang, J. Gao and D. J. Li, *J. Alloys Compd.*, 2014, **603**, 224.
28 D. R Patil and B. K Chougule, Effect of copper substitution on electrical and magnetic properties of $NiFe_2O_4$ ferrite, *Mater. Chem. Phys.*, 2009, **117**, 35.
29 D. R. Patil, S. A. Lokare, R. S. Devan, S. S. Chougule, Y. D. Kolekar and B. K. Chougule, *J. Phys. Chem. Solids*, 2007, **68**, 1522.
30 H. Ghoudi, S. Chkoundali, Z. Raddaoui and A. Aydi, *RSC Adv.*, 2019, **9**, 25358.
31 H. Slimi, A. Oueslati and A. Aydi, *RSC Adv.*, 2021, **11**, 14504.

32 M. Bourguiba, Z. Raddaoui, M. Chafraa and J. Dhahri, *RSC Adv.*, 2019, **9**, 42252.
33 M. ben Abdessalem, A. Aydi and N. Abdelmoula, *J. Alloys Compd.*, 2019, **774**, 685–693.
34 M. A. Ahmed, S. F. Mansour, S. I. El-Dek and M. MKaramany, *J. Rare Earths*, 2016, **34**, 495.
35 Y. Chaudhari, C. M. Mahajan, A. Singh, P. Jagtap, R. Chatterjee and S. Bendre, *J. Magn. Magn. Mater.*, 2015, **395**, 329.
36 E. Cai, Q. Liu, S. Zhou, Y. Zhu and A. Xue, *J. Alloys Compd.*, 2017, **726**, 1168.
37 A. Chaudhuri and K. Mandal, *Mater. Res. Bull.*, 2012, **47**, 1057.
38 R. Bellouz, M. Oumezzine, A. Dinia, G. Schmerber, E. l.-K. Hlil and M. Oumezzine, *RSC Adv.*, 2015, **5**, 64557–64565.
39 Y. K. Jun, W. T. Moon, C. M. Chang, H. S. Kim, H. S. Ryu, J. W. Kim, K. H. Kim and S. H. Hong, *Solid State Commun.*, 2005, **135**, 133.
40 T. S. Irvine, D. C. Sinclair and A. R. West, *Adv. Mater.*, 1990, **2**, 132–138.
41 L. Miladi, A. Oueslati and K. Guidara, *RSC Adv.*, 2016, **6**, 83280–83287.
42 A. K. Jonscher, *Dielectric Relaxation in Solids*, Chelesa Dielectric Press, London, 1983.
43 P. H. Xiang, Y. Kinemuchi, T. Nagaoka and K. Watari, *Mater. Lett.*, 2005, **59**, 3590.
44 M. ben Abdessalem, A. Aydi and N. Abdelmoula, *J. Alloys Compd.*, 2019, **774**, 685–693.
45 E. Barsoukov and J. R. Macdonald, *Impedance Spectroscopy : Theory, Experiment, and Applications*, Wiley Interscience, New York, 2nd edn, 2005, p. 14.
46 J. B. Jorcin, M. E. Orazem, N. Pebere and B. Tribollet, *Electrochim. Acta*, 2006, **51**, 1473–1479.
47 R. K. Mishra, D. K. Pradhan, R. N. P. Choudhary and A. Banerjee, *J. Phys.: Condens. Matter*, 2008, **20**, 045218.
48 A. Ruff, S. Krohns, F. Schrettle, V. Tsurkan, P. Lunkenheimer and A. Loidl, Absence of polar order in $LuFe_2O_4$, *Eur. Phys. J. B*, 2012, **85**, 290.
49 F. S. Howel, R. A. Bose, P. B. Maado and C. T. Moynihan, *J. Phys. Chem.*, 1974, **78**, 639–648.
50 I. Coondoo, N. Panwar, M. A. Rafiq, V. S. Puli, M. N. Rafiq and R. S. Katiyar, *Ceram. Int.*, 2014, **40**, 9895–9902.
51 N. Sdiri, R. Jemai, M. Bejar, M. Hussein, K. Khirouni, E. Dhahri and S. Mazen, *Solid State Commun.*, 2008, **148**, 577–581.
52 J. Suchanicz, *Mater. Sci. Eng. B, Solid-State Mater. Adv. Technol*, 1998, **55**, 114.
53 M. Tachibana, *Solid State Commun.*, 2015, **221**, 33–35.
54 M. Idrees, M. Nadeem and M. M. Hassan, *J. Phys. D: Appl. Phys.*, 2010, **43**, 155401.
55 M. Younes, M. Nadeem, M. Atif and R. Grossinger, *J. Appl. Phys.*, 2010, **109**, 93704.
56 M. Nadeem and M. J. Akhtar, *J. Appl. Phys.*, 2008, **104**, 103713.
57 S. Brahma, R. N. P. Choudhary and S. A. Shivashankar, *J. Phys. Chem. Solids*, 2012, **73**, 357.
58 F. Yakuphanoglu, Y. Aydogdu, U. Schatzschneider and E. Rentschler, *Solid State Commun.*, 2003, **128**, 63.
59 A. K. Jonscher and M. S. Frost, *Thin Solid Films*, 1976, **37**(2), 267.
60 Y. Moualhi, R. M'nassri, H. Rahmouni, M. Gassoumi and K. Khirounic, *RSC Adv.*, 2020, **10**, 33868.
61 A. K. Jonscher, *Nature*, 1977, **267**, 673.
62 M. Ben Bechir, K. Karoui, M. Tabellout, K. Guidara and A. Ben Rhaiem, *J. Alloys Compd.*, 2014, **588**, 551.
63 N. F. Mott and E. A. Davis, *Electronic Process in Non-crystalline Materials*, Clarendon Press, Oxford, 1979.
64 P. C. Sati, M. Arora, S. Chauhan, M. Kumar and S. Choker, *Ceram. Int.*, 2014, **40**, 7805.
65 M. M. Costa, G. F. M. Pires-Junior and A. S. B. Sombra Mater, *Chem. Phys.*, 2010, **123**, 35.
66 P. B. Macedo, C. T. Moynihan and N. L. Laberge, *Phys. Chem. Glasses*, 1973, **14**, 122.
67 R. Das and R. N. P. Choudhary, *Solid State Sci.*, 2019, **87**, 1–8.
68 M. M. Costa, G. F. M. Pires, A. J. Terezo, M. P. F. Grac and A. S. B. Sombra, *J. Appl. Phys.*, 2011, **110**(1–7), 034107.
69 C. T. Moynihan, L. P. Boesch and N. L. Laberge, *Phys. Chem. Glasses*, 1973, **14**, 122–125.
70 D. C. Sinclair and A. R. West, *J. Appl. Phys.*, 1989, **66**, 3850–3856.